(Received 9 December 2024, Accepted 13 March 2025, Scheduled 26 March 2025)

Efficient Design of a Novel Multibeam Antenna Using Scalar Metasurfaces

Mounia Djoudi[1], Mohamed Lamine Tounsi[2], Julien Sarrazin[3, 4], and Massimiliano Casaletti[3, 4, *]

[1] *Instrumentation Laboratory, U.S.T.H.B University, Algiers, Algeria*
[2] *LCDEP Laboratory, U.S.T.H.B University, Algiers, Algeria*
[3] *Sorbonne Université, CNRS, Laboratoire de Génie Electrique et Electronique de Paris, 75252, Paris, France*
[4] *Université Paris-Saclay, Centrale Supélec, CNRS, Laboratoire de Génie Electrique et Electronique de Paris, Gif-sur-Yvette, France*

ABSTRACT: This paper presents a simple and innovative approach for the design of multibeam scalar metasurface antennas. The proposed method, based on the equivalent currents on the antenna aperture, allows beams to be radiated in arbitrary directions with the desired polarization. Unlike other solutions available in the literature, this approach uses scalar metasurfaces, which are much simpler to implement than tensor ones, and also do not require optimizations through ad hoc developed numerical analysis tools. Analytical design equations based on the physics are introduced, and a block diagram for the designs of such antennas is presented. Two antenna designs are presented, and the corresponding numerical results demonstrate the flexibility of the presented method. A prototype of a two-beam antenna with orthogonal circular polarizations, operating at 20 GHz, was fabricated and measured. These results confirm the effectiveness of scalar metasurfaces in creating multibeam patterns, paving the way for various applications in advanced communication systems.

1. INTRODUCTION

Metasurfaces (MTSs) have recently emerged as a considerable advancement in the fields of optics and telecommunications, offering precise control over the propagation of electromagnetic (EM) waves. These ultrathin two-dimensional structures, intricately designed with periodic sub-wavelength patterns, represent a cutting-edge innovation in contemporary technology [1]. Their close connection to photonic crystals places them at the forefront of research, sharing fundamental characteristics [2–6].

Metasurfaces enable detailed manipulation of EM waves attributes such as phase, amplitude, and polarization, leading to a variety of promising applications including holographic antennas and leaky-wave (LW) devices [7, 8], demonstrating novel methods of wave control widely applicable across various sectors, including metasurface lenses for high-resolution imaging [9, 10], phase modulators for detection systems [11], telecommunications such as smart antennas for 5G/6G networks [12], metasurface filters for advanced wireless communications [13, 14], and metasurface reflectors for enhancing beamforming [15].

The pioneering works of Oliner and Hessel [16] introduced the concept of surface wave (SW) extension adapted to modulate surface impedance while Fong et al. [17], presented holographic metasurface antennas. By judiciously choosing an appropriate modulated surface impedance, it is possible to control SW propagation or achieve SW-to-LW transition, opening new challenges in antenna and optical device design [18, 19]. Additional research groups have extended these techniques [8, 20, 21], going so far as to obtain multibeam antennas in far- [22–24] and near-field regions [25] with polarization control. The resulting antennas are realized by printing a metasurface on a single dielectric substrate and connectorizing the back of the substrate. They represent thin and cheap multibeam solutions that can be used in low-cost multiple-input multiple-output (MIMO) sensing applications, wireless communications, including satellite systems [26] and next-generation wireless networks [27].

However, these design methods for complete control of the direction and polarization of the beam radiated by the antenna require the use of tensor metasurfaces and extensive numerical optimization based on proprietary analysis codes [28, 29]. These aspects limit the use of such techniques because of either the unavailability of such dedicated tools or the difficulty in realizing and characterizing tensor metasurfaces.

In this paper, we present a simple approach to the design of a holographic scalar metasurface antenna able to radiate multiple beams in the far-field region at arbitrary directions with the desired polarization. Scalar metasurfaces have been widely studied in the literature and realized in different technologies so that their realization is affordable by not requiring the development of dedicated tools. Analytical design equations based on the antenna aperture field are introduced, and a flowchart for the designs of such antennas is presented.

Two antenna designs are presented radiating two and four beams, respectively. The obtained numerical results validate the presented method. A prototype of a two-beam antenna with

* Corresponding author: Massiliano Casaletti (massimiliano.casaletti@sorbonne-universite.fr).

orthogonal circular polarizations, operating at 20 GHz, was fabricated and experimentally validated.

This paper is structured as follows. Section 2 summarizes the basic phenomenology and design guidelines. Section 3 introduces the antenna design procedure. Section 4 presents the design of two antennas and numerical/experimental results. Finally, a conclusion is presented in Section 5 including some perspectives.

2. SCALAR MTS DESIGN OF MULTIBEAM ANTENNA

2.1. Theoretical Foundation

The proposed MultiBeam Antenna (MBA) is illustrated in Fig. 1. A feeder generates a cylindrical surface wave that propagates along the metasurface which consists of a periodic structure of conductive elements printed on a dielectric substrate. To describe the EM behavior of the metasurface, we use the concept of equivalent scalar surface impedance Z_s. In the context of antennas, spatially modulating Z_s allows to control the propagation of surface waves. More specifically, we focus on the transformation of a surface wave (SW) into a fast wave, i.e., a Leaky Wave (LW) [30].

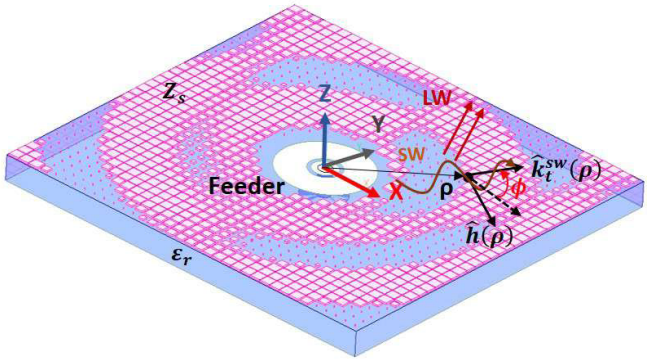

FIGURE 1. General geometry of metasurfaces: SW propagation conversion to LW.

Let us consider a feeder emitting an incident SW propagating in a general direction onto a metasurface placed in the xy-plane (Fig. 1). For a lossless scalar inductive surface impedance defined by $Z_s = j\bar{X}_s$ where ($\bar{X}_s > 0$), the dominant SW mode is a TMz mode (where z is normal to the surface, and TM stands for transverse magnetic). The magnetic field at the surface can be expressed as follows [21]:

$$\mathbf{H}_{\text{inc}}{}^{\text{aperture}}(\boldsymbol{\rho}) = A_{TM}(\boldsymbol{\rho})e^{-j\mathbf{k}_t^{sw}(\boldsymbol{\rho})\cdot\boldsymbol{\rho}}\hat{\mathbf{h}}(\boldsymbol{\rho}) \tag{1}$$

where $\boldsymbol{\rho} = x\hat{\mathbf{x}} + y\hat{\mathbf{y}}$ is a general point on the antenna surface; A_{TM} is the amplitude; $\hat{\mathbf{h}}$ is the unit polarization vector; $\mathbf{k_t^{sw}} = k_t^{sw}\hat{\mathbf{k}}_\mathbf{t}^{\mathbf{sw}}$; and $\hat{\mathbf{k}}_\mathbf{t}^{\mathbf{sw}}$ defines the propagation direction [30]. The corresponding propagation constant k_t^{sw} is obtained by solving the transverse dispersion problem [31]:

$$k_t^{sw} = k_0\sqrt{1 + \left(\bar{X}_s(\mathbf{k}_\mathbf{t}^{\mathbf{sw}})/\zeta\right)^2} > k_0 \tag{2}$$

where ζ is the impedance of free space, and $k_0 = \omega\sqrt{\epsilon_0\mu_0}$. The tangential electric field is obtained by applying the scalar impedance boundary condition given by:

$$\mathbf{E}_{\text{inc}}^{\text{aperture}}(\boldsymbol{\rho}) = -A_{TM}(\boldsymbol{\rho})Z_s(\boldsymbol{\rho})\hat{\mathbf{z}}\times\hat{\mathbf{h}}(\boldsymbol{\rho})e^{-j\mathbf{k}_t{}^{sw}(\boldsymbol{\rho})\cdot\boldsymbol{\rho}} \tag{3}$$

Now, consider a periodic modulation of the surface impedance in the propagation direction, expressed as [30]:

$$Z_s(\boldsymbol{\rho}) = j\bar{X}_s\left(1 + M(\rho)\cos\left(\frac{2\pi}{p(\rho)}\mathbf{k}_t^{sw}(\rho).\boldsymbol{\rho}\right)\right) \tag{4}$$

where M is the modulation index, and p represents the periodicity. When $M \ll 1$, this modulation constitutes a perturbation boundary condition, allowing the use of a quasi-geometric optic approximation to address the propagation problem [8, 19].

The dispersion relation is replaced by a continued fraction equation [16], resulting in a complex propagation constant k_t. This constant indicates that some energy radiates into space as a leaky wave (LW). The modulated propagation constant $k_t(\boldsymbol{\rho})$ can be effectively approximated by the surface wave propagation constant $k_t^{sw}(\boldsymbol{\rho})$, simplifying the modeling of wave propagation and radiation.

2.2. Radiated Fields from Surface Modulations

The locally modulated metasurface can be described by surface currents as follows [30]:

$$\begin{aligned}\mathbf{J}_M(\boldsymbol{\rho}) &= 2\mathbf{E}(\boldsymbol{\rho})\times\hat{\mathbf{z}}\\ &= -2A_{TM}(\boldsymbol{\rho})Z_s(\boldsymbol{\rho})e^{-j\mathbf{k}_t(\boldsymbol{\rho})\cdot\boldsymbol{\rho}}\hat{\mathbf{h}}\end{aligned} \tag{5}$$

where $\mathbf{J_M}(\boldsymbol{\rho})$ is the equivalent magnetic current. By substituting the expression for Z_s, we obtain:

$$\mathbf{J}_M(\boldsymbol{\rho}) = \mathbf{J}_M^{(0)}(\boldsymbol{\rho}) + \mathbf{J}_M^{(-1)}(\boldsymbol{\rho}) + \mathbf{J}_M^{(1)}(\boldsymbol{\rho}) \tag{6}$$

where the first and third terms represent non-radiative surface wave (SW) currents, and the second term can be radiative if $k_t(\boldsymbol{\rho}) - \frac{2\pi}{p(\boldsymbol{\rho})} < k_0$ [18]. By locally varying the impedance period $p(\boldsymbol{\rho})$, SWs can be transformed into radiative waves (LW) in a desired direction. The far-field radiation is determined using [30]:

$$\mathbf{E}_{FF}(\theta,\phi) = jk_0\iint_S \hat{\mathbf{r}}(\theta,\phi)\times\mathbf{J}_M^{(-1)}(\boldsymbol{\rho})e^{jk_0\boldsymbol{\rho}\cdot\hat{\mathbf{r}}}d\boldsymbol{\rho} \tag{7}$$

To achieve a specific radiation pattern, the metasurface period $p(\boldsymbol{\rho})$, average impedance $\bar{X}_s$, and modulation index M are optimized. The methodology for tailoring these parameters to achieve desired beam directions and polarizations is detailed in [30] and [32].

2.3. Far-Field Multibeams Antenna

The design of scalar metasurface antennas is critical for generating well-polarized beams in both the far-field and near-field zones. We assume that the feeder can be approximated as a point source located at the origin, resulting in an incident SW characterized by a cylindrical wavefront [30]:

$$\mathbf{H}_{\text{inc}}^{\text{aperture}}(\boldsymbol{\rho}) = A_{\text{TM}}H_1^{(2)}(k_t\rho)\hat{\phi} \tag{8}$$

The corresponding equivalent magnetic current is directed in the $\hat{\phi}$ direction:

$$\mathbf{J}_M(\boldsymbol{\rho}) = A_{\text{TM}} Z_s(\boldsymbol{\rho}) H_1^{(2)}(k_t(r)\rho)\hat{\boldsymbol{\phi}} \tag{9}$$

This formulation allows the modulation of the surface impedance, which is essential to extracting the radiation patterns of the antenna.

To generate a circularly polarized (CP) beam pointing at θ_0 and ϕ_0, we use the following azimuthal magnetic current distribution:

$$\mathbf{J}_M(\rho', \phi') = e^{\pm j\phi'} e^{-jk_0\rho' \sin\theta_0 \cos(\phi'-\phi_0)}\hat{\boldsymbol{\phi}} \tag{10}$$

In this context, the upper (+) and lower (-) indices correspond to left-hand and right-hand circular polarizations, respectively. The linear phasing described in (10) ensures coherent optical paths for each surface current element directed toward the intended point. Additionally, the term $e^{\pm j\phi}$ effectively manages the polarization [30].

Using the previous results, a multiple beams pattern antenna could be obtained by using as aperture magnetic currents a summation of terms of the form (10) as:

$$\mathbf{J}_M(\rho', \phi') = \sum_{n=1}^{N_{\text{beams}}} e^{\pm j\phi'} e^{-jk_0\rho' \sin\theta_n \cos(\phi'-\phi_n)}\hat{\boldsymbol{\phi}} \tag{11}$$

where N_{beams} represents the total numbers on beams and (θ_n, ϕ_n) the direction of the n-th beam, while the polarization is selected by acting on the $e^{\pm j\phi'}$ term. In the previous formula, linearly polarized beams can be created as a linear combination of two CP beams in the same direction having orthogonal polarizations.

The corresponding impedance law can be derived substituting the following relation in Equation (4):

$$\begin{aligned}
&\cos\left(\frac{2\pi}{p(\rho)}\rho\right) \\
&= \text{Re}\left\{e^{j\text{Arg}[H_1^{(2)}(k_t\rho)]} \sum_{n=1}^{N_{\text{beams}}} e^{\mp j\phi} e^{-jk_0\rho \sin\theta_n \cos(\phi-\phi_n)}\right\} \\
&= \sum_{n=1}^{N_{\text{beams}}} \cos\left(k_t\rho + k_0\rho \sin\theta_n \cos(\phi-\phi_n) \pm j\phi\right)
\end{aligned} \tag{12}$$

Leading to:

$$\begin{aligned}
&Z_s(\rho) \\
&= j\bar{X}_s\left(1 + M(\rho)\sum_{n=1}^{N_{beams}} \cos\left(k_t\rho + k_0\rho \sin\theta_n \cos(\phi-\phi_n) \pm j\phi\right)\right)
\end{aligned} \tag{13}$$

By employing this latter expression, it is possible to design scalar metasurface antenna able to radiate multiple beams with different polarizations and directions. The physical implementation of the previous impedance can be done using squared patches thanks to a numerical optimization or using analytical formulas available in the literature as presented in [33].

The far-field radiation pattern is directly impacted by the local impedance modulation via the radiation Fourier-type integral (7). At each surface point, the impedance is determined by three key parameters: average impedance ($\bar{X}_s$), modulation index (M), and spatial period (p). All of these parameters define the propagation constant (k_t). The modulation index (M) must remain small ($M < 1$) so that the modulation represents a small perturbation of the mean impedance and verifies the assumptions of Subsection 2.1. Furthermore, the product $\bar{X}_s \cdot M$ impacts the amplitude of the aperture field amplitude, while the spatial period (p) primarily controls its phase. This interplay enables the precise tailoring of the radiation pattern. Further insights into these mechanisms can be found in [32].

3. ANTENNA DESIGN PROCEDURE

3.1. Scalar Metasurface Design Process

The metasurface implementing the impedance boundary condition is realized by printing a periodic pattern (with period D) of square metallic patches of size w on a dielectric substrate of height h and relative dielectric constant ϵ_r. The geometry and the equivalent transmission line for TMz mode are shown in Fig. 2.

The grounded dielectric substrate is equivalent to a short-circuited transmission line of length h and characteristic impedance $Z_d^{TM}(k_t) = \zeta_0\sqrt{k_0^2\varepsilon_r - k_t^2}/k_0\varepsilon_r$, and the free half-space above the metasurface is described by a semi-infinite transmission line of impedance $Z_0^{TM}(k_t) = \zeta_0\sqrt{k_0^2 - k_t^2}/k_0$. Finally, the patches are described by an equivalent lumped element Z_{grid}^{TM}. This latter can be rigorously found by full-wave numerical analysis of the periodic grid or, in the case of square patches, by analytical formulas [33]:

$$Z_{\text{grid}}^{TM} = j\frac{\pi\eta_0}{k_0(\varepsilon_r+1)D\ln\left(\sin\left(\frac{\pi w}{2D}\right)\right)} \tag{14}$$

Therefore, the total impedance of the metasurface Z_s is given by

$$Z_s(k_t) = \frac{jZ_{\text{grid}}^{TM} Z_d^{TM}(k_t)\tan\left(\sqrt{k_0^2\varepsilon_r - k_t^2}h\right)}{Z_{\text{grid}}^{TM} + jZ_d^{TM}(k_t)\tan\left(\sqrt{k_0^2\varepsilon_r - k_t^2}h\right)} \tag{15}$$

The previous expression depends on the propagation constant k_t. To determine the impedance relative to the surface wave, we must first determine the wave number relative to the surface wave by imposing the transverse resonance of the transmission line:

$$\begin{aligned}
&Z_s(k_t^{\text{sw}}) + Z_0^{TM}(k_t^{\text{sw}}) = 0 \implies \\
&\frac{jZ_{grid}^{TM} Z_d^{TM}(k_t^{sw})\tan\left(\sqrt{k_0^2\varepsilon_r - k_t^{sw2}}h\right)}{Z_{grid}^{TM} + jZ_d^{TM}(k_t^{sw})\tan\left(\sqrt{k_0^2\varepsilon_r - k_t^{sw2}}h\right)} + \frac{\zeta_0\sqrt{k_0^2 - k_t^{sw2}}}{k_0} = 0
\end{aligned} \tag{16}$$

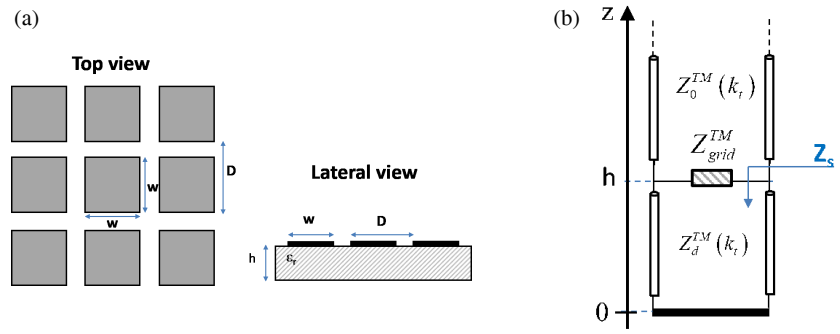

FIGURE 2. (a) Geometry of the metasurface. (b) Equivalent TMz transmission line.

The previous equation must be solved numerically, after which the metasurface impedance is obtained from Equation (15) as $Z_s(k_t^{\text{sw}})$.

For our application at the working frequency of 20 GHz, we used the low-cost dielectric substrate FR-4 with a relative permittivity of $\varepsilon_r = 4.7$ and a thickness of $h = 1.6\,\text{mm}$. The period D must be smaller than half a wavelength in both media to have only one propagating plane wave. Our choice was to use a period $D = \frac{\lambda_0}{15} - \frac{\lambda_d}{7} = 1\,\text{mm}$. The obtained impedance as a function of the filling factor (w/D) for the TM_z surface wave is reported in Fig. 3.

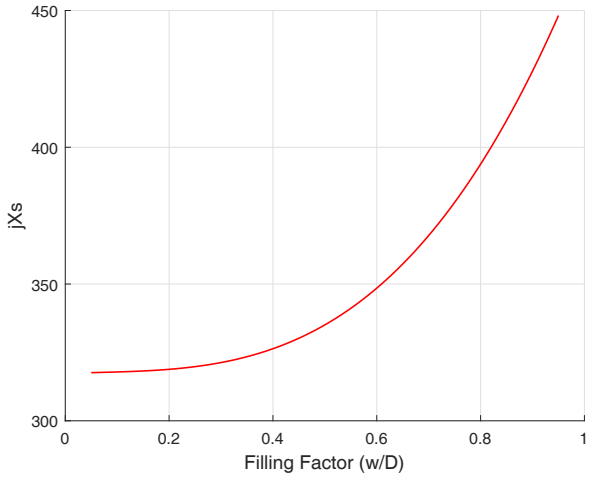

FIGURE 3. Equivalent metasurface impedance as a function of the filling factor w/D.

We must now make a proper choice of average impedance $\bar{X}_s$. Typical values of M modulation indices of metasurface antennas range between 0.05 and 0.35 [8, 17, 18, 21, 30]. We thus chose $\bar{X}_s = 382$ ($D = 0.762\,\text{mm}$) so that we could cover the dynamics of the impedance values needed for a modulation index $M \leq 0.2$.

3.2. Design of the Feeder

The geometry of the feeder is shown in Fig. 4. A circular patch of radius r_2 is excited at the center by a coaxial cable. An annular slot of width w and centered at r_1 is added to add geometrical degrees of freedom for the antenna matching. A parametric optimization was performed using the commercial software Ansys HFSS. To speed up the process, we considered a simpler geometry composed of the feeder surrounded by a limited portion of the metasurface, then adding absorbing boundary conditions. Each geometrical parameter was individually analyzed to assess its influence on antenna matching.

Figure 5 shows the influence of the outer patch radius $R2$ on the reflection coefficient $|S_{11}|$ while keeping the other parameters fixed ($r_1 = 1.17\,\text{mm}$, $w = 0.38\,\text{mm}$). The curves show that a change in parameter r_2 causes a significant shift in the resonant frequency.

The effect of changes in the inner radius r_1 is shown in Fig. 6 ($r_2 = 4.2\,\text{mm}$, $w = 0.38\,\text{mm}$). The results indicate that r_1 has a small impact on the resonance frequency, but still manages to change the amplitude of $|S_{11}|$. These aspects suggest that it could be used for final fine-tuning.

Figure 7 presents the variation of the reflection coefficient $|S_{11}|$ in dB for different values of the slot's width w. This geometrical parameter primarily affects the amplitude of $|S_{11}|$ close to the resonance, while its influence on the resonant frequency itself is minimal.

To summarize, the antenna matching is done by initially imposing the central resonant frequency by a proper choice of the parameter r_2, and then minimizing the $|S_{11}|$ acting on the parameters w and r_1. After this procedure, we selected the following geometrical parameters $(r_1, r_2, w) = (1.17; 4.2; 0.35)$.

3.3. Antenna Design Flowchart

The flowchart in Fig. 8 summarizes the design process of the multibeam scalar metasurface antenna. The described algorithm was implemented in a MATLAB code. Intermedial (for feeder optimization) and the final geometries were exported in a DXF (Drawing eXchange Format) file and subsequently imported into commercial analysis software.

4. SIMULATION AND EXPERIMENTAL RESULTS

4.1. Two-Beam MTS Antenna Simulation and Measurements

This section presents an antenna radiating two beams with orthogonal circular polarization (RHCP and LHCP) at two different angles ($\theta_1 = -25°$, $\phi_1 = 0°$), ($\theta_2 = 15°$, $\phi_2 = 0°$) working at 20 GHz. The metasurface antenna has a radius of

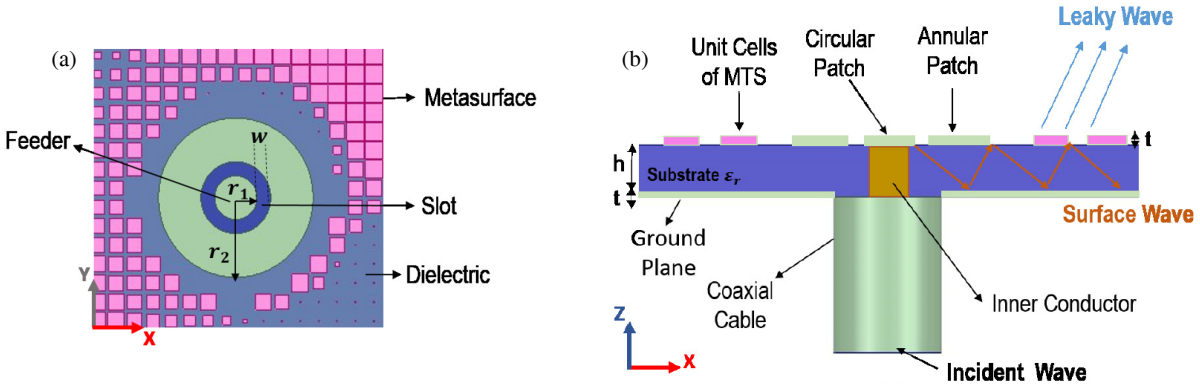

FIGURE 4. Overview of feeder structure: aerial and frontal views.

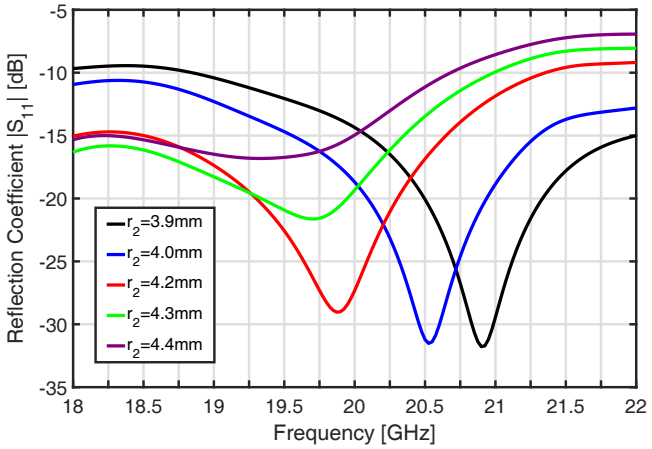

FIGURE 5. Reflection coefficient magnitude $|S_{11}|$ in dB for different outer patch radius (r_2) with constant feeder geometric parameters ($r_1 = 1.17$ mm, $w = 0.38$ mm).

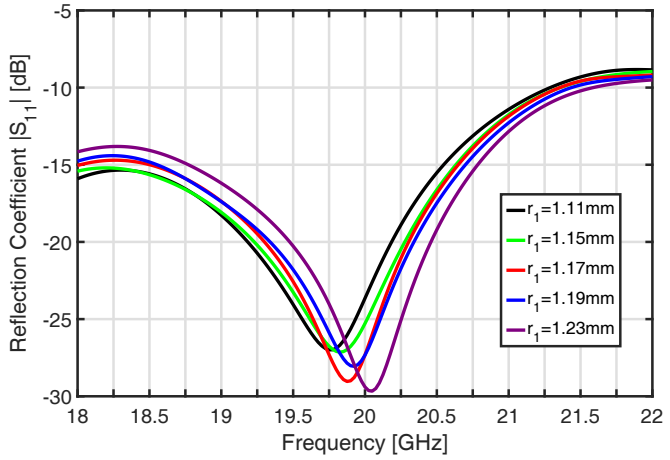

FIGURE 6. Reflection coefficient magnitude $|S_{11}|$ in dB for different inner patch radius (r_1) with constant feeder geometric parameters ($r_2 = 4.2$ mm, $w = 0.38$ mm).

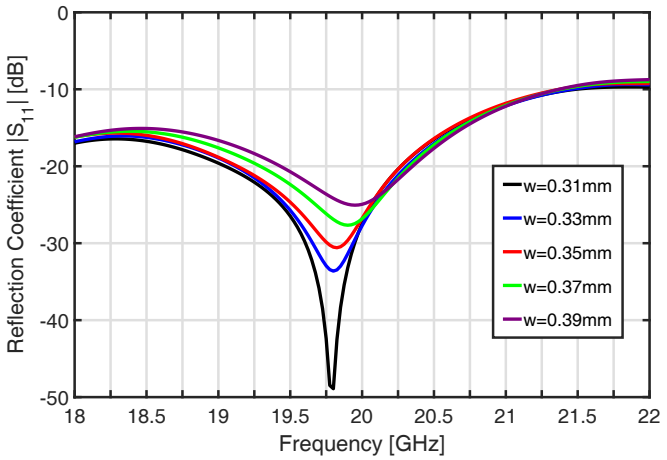

FIGURE 7. Frequency-dependent variation of reflection coefficient magnitude $|S_{11}|$ in dB for different annular slot widths (w) with constant feeder geometric parameters ($r_2 = 4.2$ mm, $r_1 = 1.17$ mm).

6 wavelengths (90 mm) and has been implemented by 25356 conducting elements on an FR4 substrate. The modulation index varies with linear law between the value $M_{\min} = 0.15$ at the center of the antenna and $M_{\max} = 0.2$ toward the periphery. Furthermore, in a region at the edge of the antenna, a high modulation of $M = 0.35$ is used to make sure that the surface wave is fully radiated. The antenna was simulated using HFSS and then manufactured using a laser etching machine (LPKF Proto-Laser S4). The final antenna layout and prototype are presented in Fig. 9. The measurements setup is shown in Fig. 10. Stan-

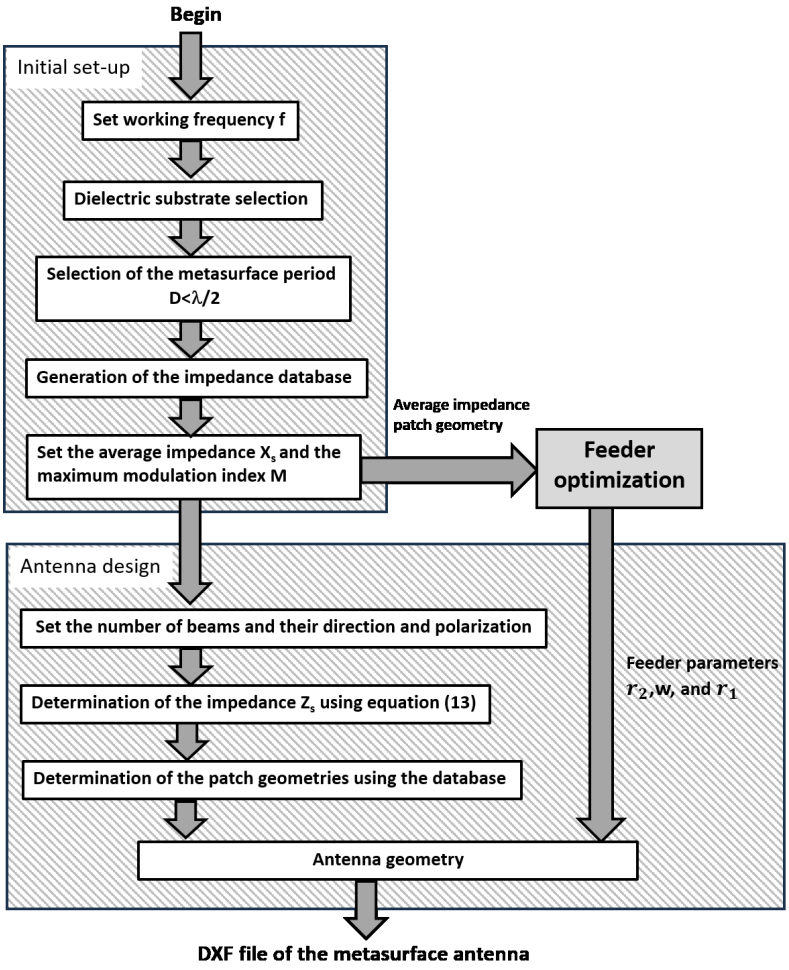

FIGURE 8. Metasurface design flowchart.

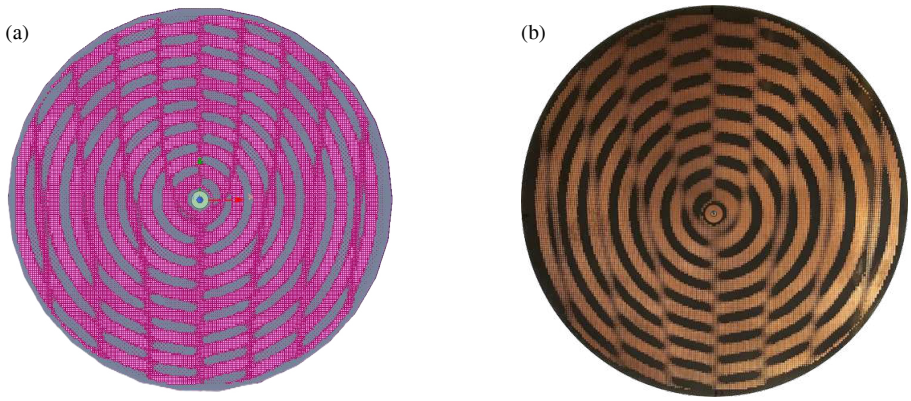

FIGURE 9. Two-beam MTS antenna final design: (a) Structure designed on Ansys HFSS designer and (b) Fabricated structure.

dard 20 dBi horn antennas were used in an anechoic chamber connected to a Rohde & Schwarz ZVA 67 GHz 4-ports vectorial network analyzer (VNA).

The results for the reflection coefficient (S_{11}) are reported in Fig. 11. The antenna is matched within a 5 GHz bandwidth around the operational frequency of 20 GHz in both simulated (red line) and measured results (dotted blue line). A frequency shift (about 1.5 GHz) is apparent between simulations and measurements probably due to the actual value of the dielectric permittivity of FR4 at 20 GHz (estimated at 4.3) compared to the nominal value of 4.7 provided by the manufacturer at 2 GHz.

Figure 12(a) presents the numerical results for the radiated gain in the $\phi = 0$ cut-plane obtained using the commercial software Altair FEKO. As expected, the radiation pattern exhibits two beams with the correct circular polarization in the expected directions (indicated by the dashed lines). Experimental results

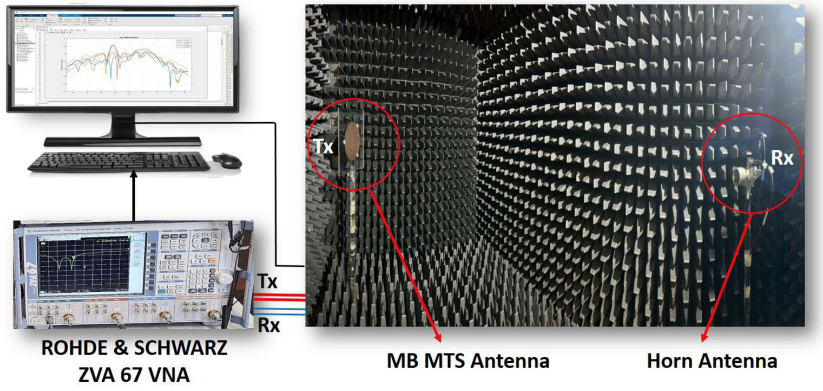

FIGURE 10. MTS antenna in the anechoic chamber.

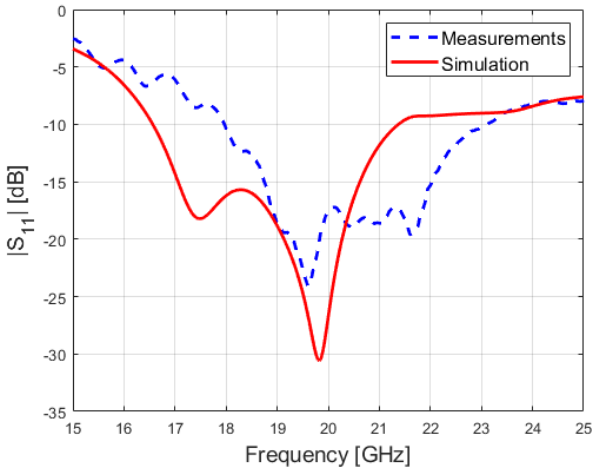

FIGURE 11. Simulated and measured S_{11} parameters.

are shown in Fig. 12(b). The measured RHCP beam is directed in the $\theta_1 = -24.1°$ direction expected $\theta_1 = -25°$ with a gain of 16.49 dBi (18.4 dBi in simulation), while the LHCP one in the $\theta_2 = 16.8°$ direction expected $\theta_2 = 15°$ with a gain equal to 15.52 dBi (18.3 dBi in simulation).

A higher level of cross-polarization than that predicted by simulations can be observed from the measurements. We also attribute this fact to the variation of the dielectric constant of the substrate. The real average impedance of the prototype at 20 GHz is different from that used in the design, which causes the surface wave to propagate with a propagation constant differing from the expected one. Since the local periodicity of the metasurface is unchanged, it implies that the holography condition is verified at a higher frequency (estimated at 20.6 GHz).

Figure 12(c) shows the gain measured at 20.6 GHz, where a lower level of cross-polarizations can be seen in both beams. The gain in the two directions of the antenna beams is higher than the numerical simulations. It is important to note that the numerical analysis of such antennas is a challenging task even for recent workstations (we used a CPU with 16 cores and 256 Mb of memory). So a compromise must be made between computation time/memory space used and mesh quality. In addition, at the operating frequency of 20.6 GHz, the radiating area of the prototype is larger in terms of wavelengths (6.2λ) than that of the simulated antenna (6λ).

Figure 13 highlights the gain observed in the frequency range 19–21.5 GHz, relative to the main beam directions. The pattern as a function of the frequency is shown in Fig. 14 where the beam's nominal directions are indicated by the dashed lines. The measured axial ratio in the beam directions is shown in Fig. 15. The 3-dB AR beamwidth for both beams is measured as 20.2 GHz–21.43 GHz. The measured aperture efficiency for each beam is shown in Fig. 16. It is important to note that this curve reports the efficiency of the prototype compared with a uniform antenna of the same size capable of radiating only one of the two beams.

4.2. Four-Beam MTS Antenna

This section presents a four-off-axis beam antenna with different polarizations: two orthogonal CP beams pointing at $\theta_1 = 25°$ and $\theta_2 = -30°$ in the $\phi = 0°$ plane and two linearly polarized (LP) beams along the ϕ direction pointing at $\theta_3 = 25°$ and $\theta_4 = -30°$ in the $\phi = 90°$ plane, respectively. As explained in Subsection 2.3, the LP is obtained by superimposing two CP beams with orthogonal polarization in the same direction, thus the value of $N_{beam} = 6$ has been used in Equation (13). The feeder and metasurface have the same size and average impedance as the previous antenna. The antenna layout and the 3D pattern provided by Altair FEKO are shown in Fig. 17. The corresponding reflection coefficient (S_{11}) is reported in Fig. 18. A good matching is obtained in the 19.3–22 GHz frequency band.

Figure 19(a) presents the antenna gain pattern simulated at 20 GHz in the $\phi = 0°$ cut-plane. The results reveal two CP beams pointing at $\theta_1 = 24.5°$ and $\theta_2 = -30.5°$. The first beam shows a maximum gain of 16.8 dBi, while the second beam achieves a maximum gain of 16.9 dBi, with a 3 dB gain bandwidth of 5°.

The $\phi = 90°$ cut-plane is reported in Fig. 19(b). The two LP beams are directed at $\theta_3 = 24.48°$ and $\theta_4 = -30°$. The third beam exhibits a maximum gain of 18.54 dBi, while the fourth beam has a maximum gain of 18.6 dBi, with a 3 dB gain band-

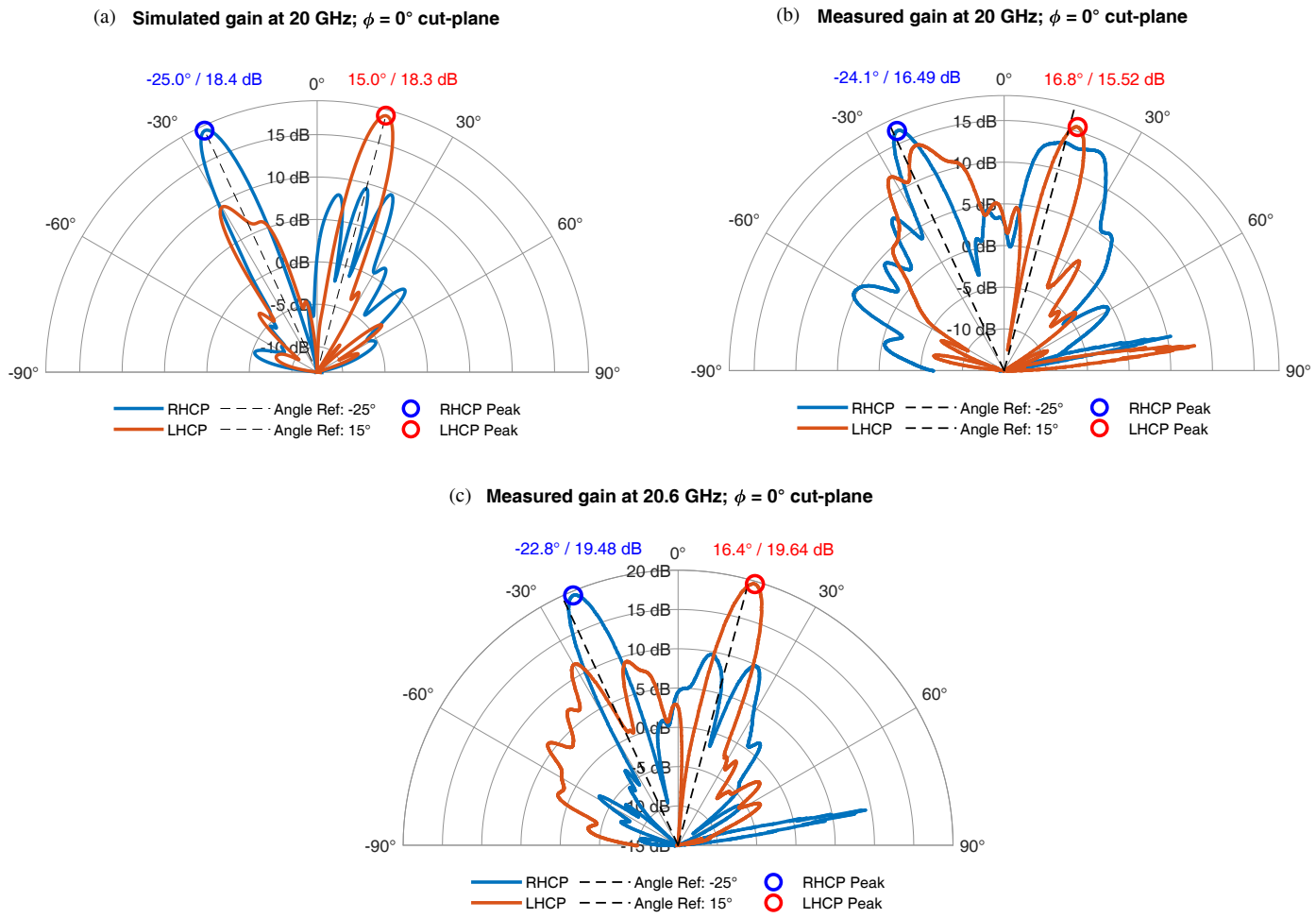

FIGURE 12. Antenna gain in the $\phi = 0°$ cut-plane. (a) Simulated gain at 20 GHz. (b) Measured gain at 20 GHz. (c) Measured gain at 20.6 GHz.

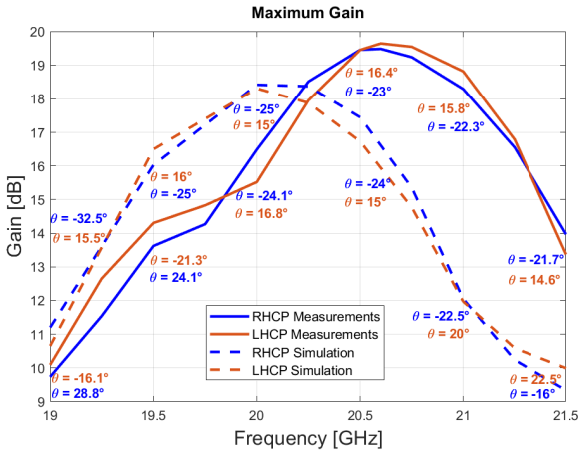

FIGURE 13. Simulated and measured maximum gains in the frequency range spanning between (19 and 21.5 GHz) with main beam directions.

width of 5.25°. The corresponding cross-polarization levels are −9.43 dB for the third beam and −9.2 dB for the fourth beam.

A small inaccuracy of the pointing angle appears when the beam deviates significantly from the broadside direction. Numerical investigation of other antenna designs confirms this kind of behavior. This fact agrees with the difficulty of radiating grazing beams with planar aperture antennas. The cross-polarization level is higher in the first beam than in the other three. Numerical investigation shows that the level of cross-polarizations is inversely proportional to antenna size. This can be explained by the fact that the beam angular width and secondary beam levels of each beam radiated by the current distribution (11) are inversely proportional to the size of the antenna.

4.3. General Performance Considerations

Table 1 provides a comparison of the measured performance of the two-beam antenna with some solutions available in the literature. As may be noted, the majority of these solutions make use of multiple ports. By optimizing the location of each port, it is possible to use the entire antenna surface almost independently of the other ports, allowing the optimization of the aperture efficiency at the expense of increasing the complexity of the antenna and control electronics. The only solution that has only one port uses a tensor metasurface. This type of metasurface, which is more technologically complex to implement, provides control over the direction of the antenna's aperture field, so in principle it allows a higher aperture efficiency than antennas using scalar metasurfaces. Our solution turns out

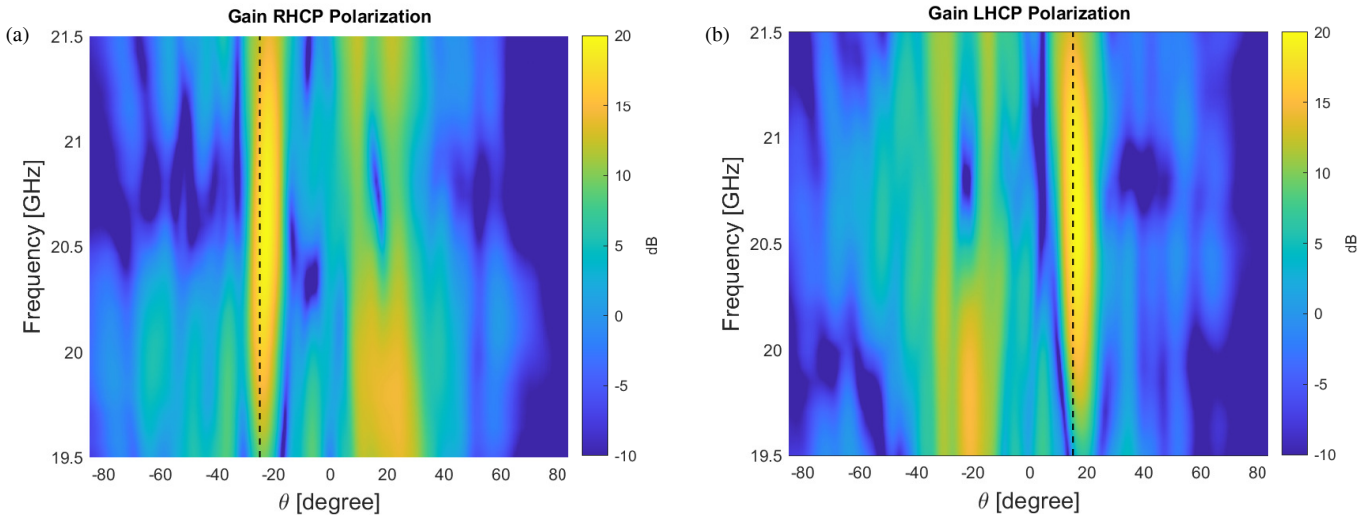

FIGURE 14. Antenna gain as a function of the frequency. (a) RHCP component. (b) LHCP component.

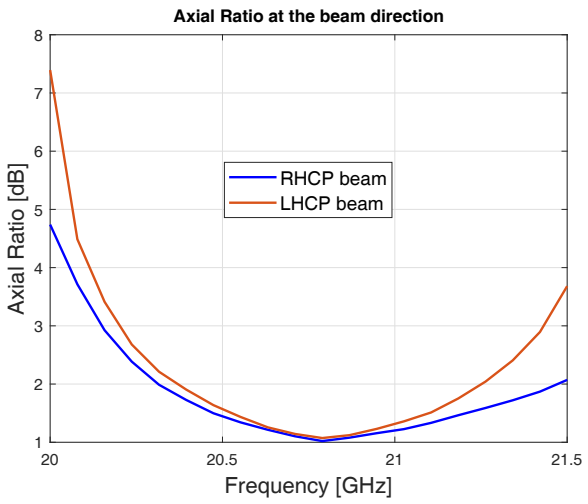

FIGURE 15. Measured axial ratio of two-beam metasurface antenna.

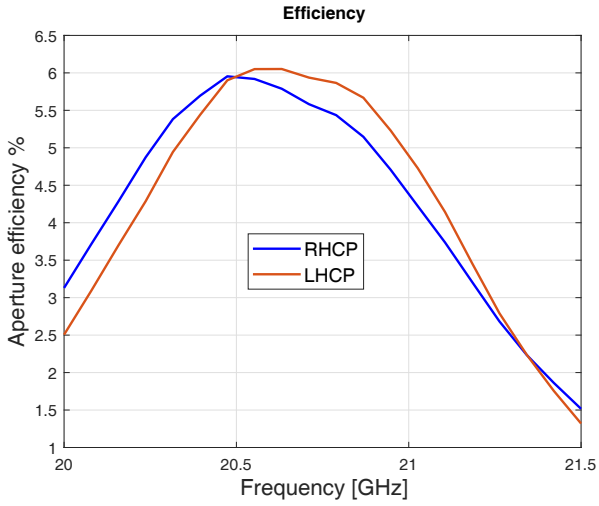

FIGURE 16. Measured aperture efficiency vs. frequency.

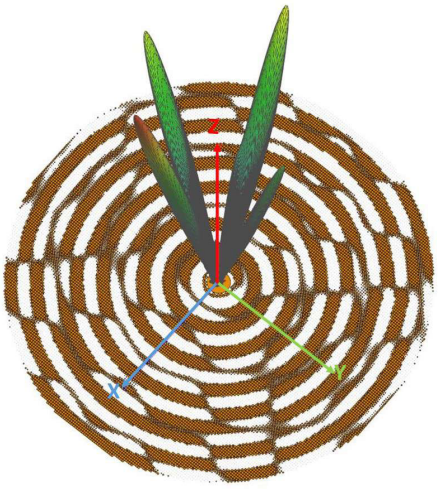

FIGURE 17. Multibeam antenna layout and 3D pattern.

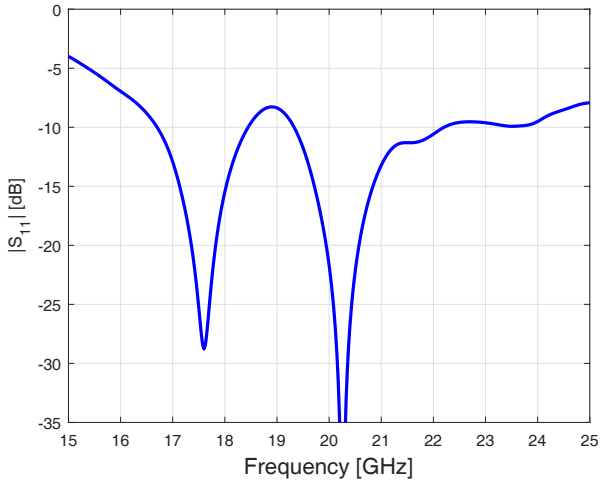

FIGURE 18. S_{11} parameter variation for the four-beam MTS antenna.

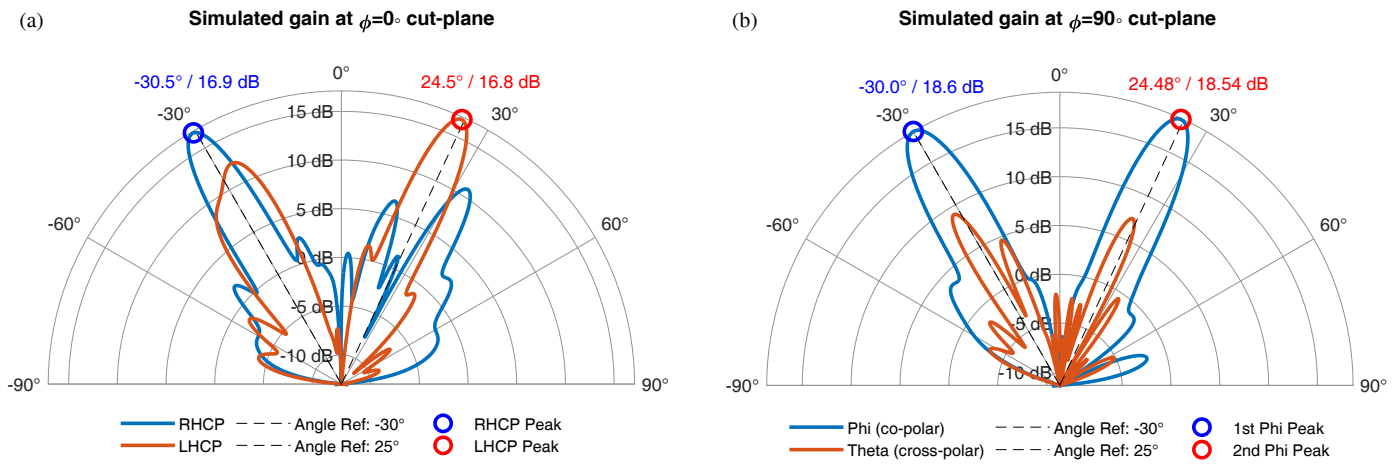

FIGURE 19. (a) Simulated right-hand circular polarization and left-hand circular polarization components. (b) Simulated theta cross polarization and phi co polarization components.

TABLE 1. Performance comparison of multibeam MTS antennas.

Ref.	Freq (GHz)	Aperture Area	Ports	Beams	Gain (dBi)	Aperture efficiency
[34]	12	$9.6\lambda_0 \times 8\lambda_0$	2	2	16	4.1%
[35]	28	$0.5\pi(9.4\lambda_0)^2$	1	1TM + 1TE	18 for TM 17.3 for TE	3.6% 3.1%
[36]	14	$10\lambda_0 \times 10\lambda_0$	7	7	20	8%
[37]	24	$\pi(10\lambda_0)^2$	4	2	21 (Simulation)	3.2% (Simulation)
[38]	17 20	$13.5\lambda_0 \times 13.5\lambda_0$ $15.9\lambda_0 \times 15.9\lambda_0$	2	2	18.3 22.4	3% 5.5%
This work	20.6	$\pi(6\lambda_0)^2$	1	1RHCP + 1LHCP	19.48 for RHCP 19.64 for LHCP	5.9% for RHCP 6.1% for LHCP

to be very competitive from a performance point of view but has the advantage of structural (single port and scaled metasurface) and design simplicity. Thus, scalar metasurface antennas can be considered an interesting solution for the realization of planar multi-beam antennas.

5. CONCLUSION

In this paper, we present a simple and innovative procedure to design multi-beam planar antennas using scalar-modulated metasurfaces. The expression of the metasurface impedance is presented in analytical form for an arbitrary number of beams and arbitrary polarization, while a numerical optimization is presented for the feeder. The resulting design procedure has been presented in a block diagram scheme. A physical prototype of a two-beam CP metasurface antenna was fabricated and tested, demonstrating a good agreement between simulated and experimental results in terms of S parameters and radiation patterns. A second antenna design, radiating four orthogonally polarized beams in different directions, was validated through numerical simulations. The future work aims to incorporate reconfigurable printed elements, to achieve dynamic control of the radiation pattern, enabling adaptive beamforming and interference mitigation.

ACKNOWLEDGEMENT

We would like to express our sincere gratitude to the GeePs Laboratory (Laboratoire de Génie Electrique et Electronique de Paris) for their invaluable support and resources throughout this research.

REFERENCES

[1] Liu, C., F. Yang, S. Xu, and M. Li, "Reconfigurable metasurface: A systematic categorization and recent advances," *Electromagnetic Science*, Vol. 1, No. 4, 1–23, 2023.

[2] Qiao, P., W. Yang, and C. J. Chang-Hasnain, "Recent advances in high-contrast metastructures, metasurfaces, and photonic crystals," *Advances in Optics and Photonics*, Vol. 10, No. 1, 180–245, 2018.

[3] Djoudi, M., M. L. Tounsi, N. Ababou, and M. C. E. Yagoub, "Analysis of electromagnetic properties of EBG structures for directional planar antennas," in *2021 International Conference on Electrical, Communication, and Computer Engineering (ICECCE)*, 1–6, Kuala Lumpur, Malaysia, Jun. 2021.

[4] Djoudi, M., M. L. Tounsi, and M. C. E. Yagoub, "Efficient design of a 2D EBG circular microstrip antenna for 5G applications," *AIJR Abstracts*, 49–50, 2024.

[5] Wang, X., M. S. Mirmoosa, V. S. Asadchy, C. Rockstuhl, S. Fan, and S. A. Tretyakov, "Metasurface-based realization of photonic time crystals," *Science Advances*, Vol. 9, No. 14, eadg7541,

2023.

[6] Liu, J.-W., G.-G. Liu, and B. Zhang, "Three-dimensional topological photonic crystals," *Progress In Electromagnetics Research*, Vol. 181, 99–112, 2024.

[7] Tan, X., R. Yang, S.-L. Chen, K. F. Chan, B. J. Chen, Z.-Q. Cui, P.-Y. Qin, Y. J. Guo, and C. H. Chan, "Highly integrated full-space coding metasurface for LP and CP waves manipulation spanning millimeter-Wave and sub-THz bands," *Journal of Lightwave Technology*, Vol. 43, No. 1, 288–298, 2025.

[8] Minatti, G., F. Caminita, M. Casaletti, and S. Maci, "Spiral leaky-wave antennas based on modulated surface impedance," *IEEE Transactions on Antennas and Propagation*, Vol. 59, No. 12, 4436–4444, 2011.

[9] Yuan, X., H. Guo, S. Zhuang, and J. Hu, "Generation and high-resolution focusing of higher-order vector beam via metasurface," *IEEE Photonics Journal*, Vol. 16, No. 6, 2024.

[10] Deng, F., Z. Guo, M. Ren, X. Su, L. Dong, Y. Liu, Y. Shi, and H. Chen, "Bessel beam generated by the zero-index metalens," *Progress In Electromagnetics Research*, Vol. 174, 89–106, 2022.

[11] Hu, R., Q. Min, X. Liu, A. Dai, J. Guo, and G. Situ, "Terahertz programmable metasurface for phase modulation based on free carrier plasma dispersion effect," *Applied Physics Letters*, Vol. 124, No. 25, 251703, 2024.

[12] Muqdad, Z. S., M. Alibakhshikenari, T. A. Elwi, Z. A. A. Hassain, B. S. Virdee, R. Sharma, S. Khan, N. T. Tokan, P. Livreri, F. Falcone, and E. Limiti, "Photonic controlled metasurface for intelligent antenna beam steering applications including 6G mobile communication systems," *AEU — International Journal of Electronics and Communications*, Vol. 166, 154652, 2023.

[13] Hong, Y.-P., I.-J. Hwang, D.-J. Yun, D.-J. Lee, and I.-H. Lee, "Design of single-layer metasurface filter by conformational space annealing algorithm for 5G mm-Wave communications," *IEEE Access*, Vol. 9, 29 764–29 774, 2021.

[14] Lin, P., C. Qian, J. Zhang, J. Chen, X. Zhu, Z. Wang, J. Huangfu, and H. Chen, "Enabling intelligent metasurfaces for semi-known input," *Progress In Electromagnetics Research*, Vol. 178, 83–91, 2023.

[15] Montaser, A. M. and K. R. Mahmoud, "Design of intelligence reflector metasurface using deep learning neural network for 6G adaptive beamforming," *IEEE Access*, Vol. 10, 117 900–117 913, 2022.

[16] Oliner, A. and A. Hessel, "Guided waves on sinusoidally-modulated reactance surfaces," *IRE Transactions on Antennas and Propagation*, Vol. 7, No. 5, 201–208, 1959.

[17] Fong, B. H., J. S. Colburn, J. J. Ottusch, J. L. Visher, and D. F. Sievenpiper, "Scalar and tensor holographic artificial impedance surfaces," *IEEE Transactions on Antennas and Propagation*, Vol. 58, No. 10, 3212–3221, Oct. 2010.

[18] Casaletti, M., G. Valerio, O. Quevedo-Teruel, and P. Burghignoli, "An overview of metasurfaces for thin antenna applications," *Comptes Rendus. Physique*, Vol. 21, No. 7-8, 659–676, 2020.

[19] Holloway, C. L., E. F. Kuester, J. A. Gordon, J. O'Hara, J. Booth, and D. R. Smith, "An overview of the theory and applications of metasurfaces: The two-dimensional equivalents of metamaterials," *IEEE Antennas and Propagation Magazine*, Vol. 54, No. 2, 10–35, 2012.

[20] Minatti, G., M. Faenzi, E. Martini, F. Caminita, P. D. Vita, D. González-Ovejero, M. Sabbadini, and S. Maci, "Modulated metasurface antennas for space: Synthesis, analysis and realizations," *IEEE Transactions on Antennas and Propagation*, Vol. 63, No. 4, 1288–1300, 2014.

[21] Teniou, M., H. Roussel, M. Serhir, N. Capet, G.-P. Piau, and M. Casaletti, "Tensorial metasurface antennas radiating polarized beams based on aperture field implementation," *International Journal of Microwave and Wireless Technologies*, Vol. 10, No. 2, 161–168, 2018.

[22] González-Ovejero, D., G. Minatti, G. Chattopadhyay, and S. Maci, "Multibeam by metasurface antennas," *IEEE Transactions on Antennas and Propagation*, Vol. 65, No. 6, 2923–2930, Jun. 2017.

[23] Teniou, M., H. Roussel, N. Capet, G.-P. Piau, and M. Casaletti, "Implementation of radiating aperture field distribution using tensorial metasurfaces," *IEEE Transactions on Antennas and Propagation*, Vol. 65, No. 11, 5895–5907, Nov. 2017.

[24] Teniou, M., H. Roussel, M. Serhir, N. Capet, G. Piau, and M. Casaletti, "Experimental validation of tensorial metasurfaces for the implementation of radiating aperture field distributions," *IEEE Transactions on Antennas and Propagation*, Vol. 67, No. 7, 4901–4906, Jul. 2019.

[25] Iliopoulos, I., M. Teniou, M. Casaletti, P. Potier, P. Pouliguen, R. Sauleau, and M. Ettorre, "Near-field multibeam generation by tensorial metasurfaces," *IEEE Transactions on Antennas and Propagation*, Vol. 67, No. 9, 6068–6075, Sep. 2019.

[26] Hasani, H., J. S. Silva, S. Capdevila, M. García-Vigueras, and J. R. Mosig, "Dual-band circularly polarized transmitarray antenna for satellite communications at (20, 30) GHz," *IEEE Transactions on Antennas and Propagation*, Vol. 67, No. 8, 5325–5333, 2019.

[27] Kwe, N. B., V. Yadav, M. Kumar, S. V. Savilov, M. Z. A. Yahya, and S. K. Singh, "A comparative study of dielectric substrate materials effects on the performance of microstrip patch antenna for 5G/6G application," *Journal of Materials Science: Materials in Electronics*, Vol. 35, No. 24, 1617, 2024.

[28] Bodehou, M., C. Craeye, E. Martini, and I. Huynen, "A quasi-direct method for the surface impedance design of modulated metasurface antennas," *IEEE Transactions on Antennas and Propagation*, Vol. 67, No. 1, 24–36, Jan. 2019.

[29] Zucchi, M., F. Vernì, M. Righero, and G. Vecchi, "Current based automated design of realizable metasurface antennas with arbitrary pattern constraints," *IEEE Transactions on Antennas and Propagation*, Vol. 71, No. 6, 4888–4902, Jun. 2023.

[30] Casaletti, M., M. Śmierzchalski, M. Ettorre, R. Sauleau, and N. Capet, "Polarized beams using scalar metasurfaces," *IEEE Transactions on Antennas and Propagation*, Vol. 64, No. 8, 3391–3400, 2016.

[31] Pozar, D. M., *Microwave Engineering*, 4th ed., Wiley, 2011.

[32] Faenzi, M., G. Minatti, D. González-Ovejero, F. Caminita, E. Martini, C. D. Giovampaola, and S. Maci, "Metasurface antennas: New models, applications and realizations," *Scientific Reports*, Vol. 9, No. 1, 10178, Jul. 2019.

[33] Luukkonen, O., C. Simovski, G. Granet, G. Goussetis, D. Lioubtchenko, A. V. Raisanen, and S. A. Tretyakov, "Simple and accurate analytical model of planar grids and high-impedance surfaces comprising metal strips or patches," *IEEE Transactions on Antennas and Propagation*, Vol. 56, No. 6, 1624–1632, Jun. 2008.

[34] Ramalingam, S., C. A. Balanis, C. R. Birtcher, and H. N. Shaman, "Polarization-diverse holographic metasurfaces," *IEEE Antennas and Wireless Propagation Letters*, Vol. 18, No. 2, 264–268, 2018.

[35] Weng, C.-K., Y.-Z. Tsai, A. Vilenskiy, and M. N. M. Kehn, "Tensor-free holographic metasurface leaky-wave multi-beam antennas with tailorable gain and polarization," *Sensors*, Vol. 24, No. 8, 2422, 2024.

[36] Wen, Y., P.-Y. Qin, S. Maci, and Y. J. Guo, "Low-profile multi-beam antenna based on modulated metasurface," *IEEE Transactions on Antennas and Propagation*, Vol. 71, No. 8, 6568–6578, 2023.

[37] Bodehou, M. and C. Craeye, "Array surface-wave launcher for the efficient generation of shaped beam and multibeam with metasurface," *IEEE Transactions on Antennas and Propagation*, Vol. 69, No. 12, 8860–8865, Dec. 2021.

[38] Li, Y., A. Li, T. Cui, and D. F. Sievenpiper, "Multiwavelength multiplexing hologram designed using impedance metasurfaces," *IEEE Transactions on Antennas and Propagation*, Vol. 66, No. 11, 6408–6413, Nov. 2018.